Non Uniform Rational B-Splines and Lagrange approximations for time-harmonic acoustic scattering: accuracy and absorbing boundary conditions

Shaima Magdaline Dsouza, Tahsin Khajah, Xavier Antoine, Stéphane Bordas, Sundararajan Natarajan

Non Uniform Rational B-Splines and Lagrange approximations for time-harmonic acoustic scattering: convergence, accuracy, absorbing boundary conditions

S.M. Dsouza[*], T. Khajah[†], X. Antoine[‡], S.P.A. Bordas[§¶‖], S. Natarajan[*]

Abstract

In this paper, the performance of the finite element method based on Lagrange basis functions and the Non Uniform Rational B-Splines (NURBS) based Iso-Geometric Analysis (IGA) are systematically studied for solving time-harmonic acoustic scattering problems. To assess their performance, the numerical examples are presented with truncated absorbing boundary conditions. In the first two examples, we eliminate the domain truncation error by applying second-order Bayliss-Gunzburger-Turkel (BGT-2) Absorbing Boundary Condition (ABC) and modifying the exact solution. Hence, the calculated error is an indicator of the numerical accuracy in the bounded computational domain with no artificial domain truncation error. Next, we apply a higher order local ABC based on the Karp's and Wilcox's far-field expansions for 2D and 3D problems, respectively. The performance of both methods in solving exterior problems is compared. The introduced auxiliary surface functions are also estimated using the corresponding basis functions. The influence of various parameters, viz., order of the approximating polynomial, number of degrees of freedom, wave number and the boundary conditions (BGT-2 and number of terms in the far-field expansions) on the accuracy and convergence rate is systematically studied. It is inferred that, irrespective of the order of the polynomial, IGA yields higher accuracy per degree of freedom when compared to the conventional finite element method with Lagrange basis.

Keywords. time-harmonic acoustic scattering; absorbing boundary conditions; far-field expansion; finite element method; isogeometric analysis; NURBS

[*]Department of Mechanical Engineering, Indian Institute of Technology Madras, Chennai-600036, India.

[†]Department of Mechanical Engineering, University of Texas at Tyler, USA.

[‡]Institut Elie Cartan de Lorraine, Université de Lorraine, Inria Nancy-Grand Est, SPHINX team, F-54506, Vandoeuvre-lès-Nancy Cedex, France.

[§]Faculté des Sciences, de la Technologie et de la Communication, University of Luxembourg, Luxembourg.

[¶]School of Engineering, Cardiff University, CF24 3AA, Wales, UK.

[‖]Institute of Research and Development, Duy Tan University, K7/25 Quang Trung, Danang, Viet Nam.

List of abbreviations.

- NURBS: Non Uniform Rational B-Splines
- IGA: Iso-Geometric Analysis
- BGT-2: second-order Bayliss-Gunzburger-Turkel
- ABC: Absorbing Boundary Condition
- SEM: Spectral Element Methods
- DOFs: Degrees of Freedom
- FEM: Finite Element Method
- FDM: Finite Difference Method
- GFD: Generalised Finite Differences
- SAFE: Semi Analytical Finite Element
- BEM: Boundary Element Method
- DDM: Domain Decomposition Method
- SBFEM: Scaled Boundary Finite Element
- CAD: Computer Aided Design
- T-Splines: a special type of NURBS
- PHT-Splines: Polynomial Splines over Hierarchical T-meshes
- PML: Perfectly Matched Layer
- Karp's Far-field Expansion: KFE
- Wilcox's Far-field Expansion: WFE
- Boundary-Value Problem: BVP

1 Introduction

Various numerical methods have been designed over the years for wave propagation arising in solid mechanics, geophysics, meteorology, acoustics and electromagnetic applications. Broadly speaking, the numerical techniques can be classified as domain and boundary based approaches.

Spectral Element Methods (SEMs) are among some of the most commonly used methods for wave propagation. The distribution of the nodes on the domain is such that oscillations can be minimised. This method requires fewer Degrees Of Freedom (DOFs) per wavelength compared to conventional Finite Element Method (FEM). The storage requirement and the computational complexity can be easily reduced by using vector and

parallel computing algorithms [1]. The Chebyshev polynomials which are typically employed minimise the dispersion error [2]. Higher accuracy is obtained compared to the low-order p-FEM (quadratic) [3]. The major drawback of SEM is its difficulties to deal with complex geometries. The Finite Difference Method (FDM) based on the Taylor series expansion is a classical way to solve the wave equation. The terms are truncated to arbitrary number and the dominant power of the truncated terms determines the accuracy. The Cartesian grids are usually necessary to obtain the solution unless Generalised Finite Differences (GFD) are used. The GFD is a meshless technique used on the domain, eliminating the mesh generation and the numerical quadrature. This results in requiring a high number of degrees of freedom to obtain higher accuracy. In the case of curved complex geometries which is a major characteristic and difficulty of scattering problems, this method cannot produce accurate results due to the well-known staircase effect [4]. The Semi Analytical Finite Element (SAFE) [5, 6] is another way of combining the advantages of numerical and analytical methods. This technique which uses Fourier Transforms to recover time-domain analysis was used to study Lamb wave propagation, whose behaviour is independent of the direction of propagation [7]. For a given accuracy, the computational cost for SAFE is less than that of FEM. The disadvantage here is that the wave propagation over complex geometrical features cannot be handled. When the geometries are complex, it is needed to make some of the approximations and assumptions which affect the accuracy. In these cases, the FEM becomes more useful.

Boundary Element Methods (BEM) are another way of solving the infinite domain problem. The method employs discretization of the boundary, thus reducing the d-dimensional problem to the $(d-1)$-dimension. The advances in the computing power has catalysed the use of this method. The fundamental solution represented by the Green's function is applied at the boundary and implicitly satisfies the Sommerfeld's radiation condition at infinity. The method can be used when the domain has a complex geometry but cannot be applied usually in heterogeneous media where the Green's function is not known. The resulting system of equations from BEM results in a dense and large linear system to resolve since the operator is nonlocal. Thus, this drastically increases the computational effort and memory storage required [8]. In addition, going to very high-order BEM schemes, most particularly for high-frequencies, still remains unclear, in particular because it is usually combined with fast iterative Krylov subspace solvers [9], preconditioners [10, 11] and matrix compression algorithms (see e.g. [12, 13]).

The domain-based approaches, in particular the FEM, rely on discretizing the bounded d-dimensional domain with non-overlapping regions and employing polynomial basis functions to approximate the unknown fields. The advantage of the FEM is that it can handle complex geometries, anisotropic properties, and requires no fundamental solution to represent the unknown fields. Depending on the differential operator, the matrices obtained are sparse, thus requiring less storage space while being very large and indefinite positive. In practice, in the difficult high-frequency regime, the FEM requires the use of very fine meshes and/or to increase the polynomial order to capture the fast oscillations of the unknown [14], increasing then the computational cost. In addition, the linear system solution is nontrivial since the system is highly indefinite positive and makes the Krylov subspace solvers diverging or slowly converging [15]. Specific Domain Decomposition Methods (DDM) such as the optimized Schwarz's DDM [16] are then necessary for solving large scale engineering and industrial problems. Finally, let us remark that another way to use both the FEM and BEM is to combine these two methods through FEM-BEM coupling strategies. Another method that shares the advantages of both the

FEM and the BEM is the scaled boundary finite element method (SBFEM) [17, 18]. Like the FEM, it does not require fundamental solution and like the BEM, only the boundary is discretized. Further, the radiation boundary condition can exactly be satisfied.

Using the Delaunay triangulation, in one minute 3 billion tetrahedral meshes can be generated using one machine. However, it usually does not provide quality meshes for analysis purposes [19]. The meshing of the Computer Aided Design (CAD) generated models is time consuming, especially optimisation of the mesh to obtain the quality mesh. The original geometry has to be consulted for the mesh adaptation or remeshing procedure in case of refinement of the solution on the given domain. Thus, the mesh generation process becomes tedious [20]. Furthermore, mesh generation in FEM takes 80% of the total analysis time, due to the lack of a direct connection with the models generated by CAD platforms. To attempt to alleviate these difficulties, IsoGeometric Analysis (IGA) was introduced in 2005 by Hughes *et al.* [21]. The idea was to construct one geometrical representation for all levels of mesh refinement. In IGA analysis, the NURBS basis used for the CAD models is also used for the solution space. The mesh directly interacts with the geometry and the remeshing process can be fully automated. This property combined with unique refinement possibilities makes IGA an attractive platform for shape optimization of devices relying on wave propagation phenomena [22, 23, 24]. One of the difficulty is that the CAD model provides only surface mesh and an extension of the surface mesh to a volumetric mesh is non trivial. The mesh requires a tensor product description and also, inhomogeneous Dirichlet boundary conditions need to be applied weakly. Adaptive meshing is another issue but can be addressed by using the other variants of NURBS, viz., T-splines and PHT-splines. Within this framework, NURBS are used as basis functions but are truncated. The performance of B-spline FEM and adaptive PHT-spline IGA for solving exterior time-harmonic acoustic problems were studied in [25, 26]. In particular, it was shown that the pollution error is well controlled for a fixed discretization density and order of the basis functions $p \geq 3$. The k-refinement strategy offers robust results and optimal convergence rate which is also achievable using conventional FEM at higher computational cost but the convergence rates remain the same as that of higher order FEM. The improved accuracy can be better achieved in k-refinement than with p-refinement for vibrations and wave propagation problems, where the solutions are smooth [27]. Therefore, in this study, we employ k-refinement IGA.

When using the IGA or the FEM for exterior problems, the unbounded domain must be truncated with an artificial/absorbing boundary condition to approximate the Sommerfeld's radiation condition and to ensure that the scattered wave is outgoing to the computational domain boundary while minimizing the spurious unphysical reflection. The two common choices of satisfying this on the truncated boundary are by employing: (a) a Perfectly Matched Layer (PML) [28, 29, 30, 31, 32, 33] or (b) an Absorbing Boundary Condition (ABC) [34, 35, 36, 37, 38, 39, 40, 41]. In PML, an additional absorbing layer is added that surrounds the computational domain. However, obtaining accurate results using PML usually demands to tune some specific physical and non-physical parameters which is far from being trivial [42]. It is especially challenging to tune these parameters when no exact solution is available for the problem under consideration. Apart from these two truncation techniques, a single infinite element [43, 44, 45] is used instead of non-reflecting boundary conditions. The basis functions of this element are in terms of radial functions of the outgoing wave. The test or the weighting function is conjugate or unconjugate to the trial function chosen. Some of the examples of these functions are Betess-Burnett unconjugated type, Burnett conjugated and Ashtey-Leis conjugated

[46, 47, 48]. For unconjugated type, the Gauss integration can be used to integrate the radial functions. For conjugated type, there is no oscillatory term and the integration can be performed analytically. The unconjugated types are less accurate at the far-field and offer higher precision at the near-field. In case of conjugated type, it is other way round. The accuracy of both methods deteriorates when the wave number increases.

The domain truncation introduces an error even at the continuous level which can be reduced by considering high-order ABCs. However, they are mostly tedious to implement and require the evaluation of higher order derivatives [49, 50]. Also, non-local high-order ABCs will result in fully populated linear system greatly reducing the sparsity of the FEM. Feng's higher order boundary condition [51] was studied within the framework of the FEM. It was inferred that the framework yielded accurate results for a larger domain of computation, which directly increases the computational cost. Another approach is to use enrichment techniques [52, 53], but from the numerical study it is shown that the truncation error had higher influence than the discretization error. Khajah *et al.* [54] employed the recently developed higher order local ABC based on the Karp's Far-field Expansion (KFE) and Wilcox's Far-field Expansion (WFE) within IGA for low to high frequencies for 2D and 3D problems, respectively. Unlike other ABCs, the salient feature of these higher order boundary conditions is that they do not require higher order derivative evaluation and hence impose no additional constraint on the regularity of the basis functions. This implies that the same basis functions can be used to estimate the field and the auxiliary ABC functions [54]. This is accomplished by introducing two families of auxiliary variables on the fictitious boundary. More recently, the KFE-ABC was used successfully to eliminate the domain truncation error in IGA collocation context [55]. To the best of the author's knowledge, the conventional Lagrange based FEM with KFE and WFE has not been studied in the literature.

The purpose of this paper is to investigate the performance and to compare the accuracy of the higher order FEM with the NURBS based IGA with and without domain truncation error. This is accomplished in three steps: (a) first, we artificially eliminate the domain truncation error in the numerical results by imposing Robin and BGT-2 absorbing boundary conditions on the artificial boundaries in duct and circular cylinder problems and, (b) later, we apply BGT-2 and KFE-ABC on the artificial boundary, and (c) compare numerical errors considering the full exact solution. In order to have a fair comparison between FEM and IGA, we compare them on the basis of the number of degrees of freedom for a given basis order. We also use tensor product meshes with equidistant nodes, Gaussian quadrature integration rule with identical number of Gaussian points and equal number of degrees of freedom. In the third part, we apply Wilcox's far-field expansion to 3D problems.

The paper is organized as follows. Section 2 presents the governing equations, the corresponding weak forms and a brief overview of the BGT-2, KFE and WFE ABCs. Section 3 presents an analysis by eliminating the domain truncation error, followed in Section 4 by a systematic parametric study on the numerical solution for the circular cylinder from low to high frequencies, that demonstrates the efficiency of the KFE-ABC. In Section 5, the higher order WFE-ABC is applied to 3D problems for illustrating the method. Major conclusions are presented in the last section.

2 Governing equations - ABCs

We denote the interior domain or the computational domain by Ω^-, defined as a d-dimensional scattering bounded domain of $\mathbb{R}^d$, with boundary $\Gamma := \partial\Omega^-$. We introduce the corresponding exterior unbounded domain of propagation $\Omega^+ := \mathbb{R}^d \backslash \overline{\Omega^-}$. Then, we assume that a Neumann boundary condition (sound-hard boundary condition) is prescribed with a function g on the boundary Γ and solve the wave field u in the following Boundary-Value Problem (BVP): find u such that

$$\begin{aligned} &\Delta u + k^2 u = 0, && \text{in} \quad \Omega^+, \\ &\partial_{\mathbf{n}} u = g && \text{on } \Gamma, \\ &\lim_{|\mathbf{x}|\to+\infty} |\mathbf{x}|^{(d-1)} \Big(\nabla u \cdot \frac{\mathbf{x}}{|\mathbf{x}|} - iku \Big) = 0, \end{aligned} \tag{1}$$

where Δ is the Laplacian operator, ∇ the gradient operator and $\mathbf{n}$ is the outwardly directed unit normal vector to Ω^-. The wave number k is related to the wavelength λ by the relation: $\lambda := 2\pi/k$. Denoting by $\mathbf{a} \cdot \mathbf{b}$ the Hermitian inner-product of two complex-valued vector fields $\mathbf{a}$ and $\mathbf{b}$, then the last equation of system (1) is known as the Sommerfeld's radiation condition [56, 57, 58] at infinity, ensuring the uniquenes of the solution to the BVP. We also define the discretization density n_λ as the number of degrees of freedom per wave length along each spatial direction.

In domain based computational methods, the Sommerfeld's radiation condition at infinity is approximately satisfied by artificial truncation of the computational domain at a fictitious boundary Σ and by replacing the Sommerfeld's condition with an ABC. The resulting bounded computational domain with boundary Γ and Σ is denoted by Ω. In what follows, we consider three types of ABCs to truncate the computational domain. We use the Dirichlet-to-Neumann map to describe the general form of the ABC:

$$\partial_{\mathbf{n}_\Sigma} u - \mathcal{B} u = 0, \quad \text{on } \Sigma. \tag{2}$$

Now, we write the weak form of equation (1) and find $u \in H^1(\Omega)$ such that

$$a(u, v) = \ell(v) \quad \forall v \ \in \ V, \tag{3}$$

with

$$a(u, v) = \int_\Omega \nabla u \cdot \nabla v - k^2 uv \, d\Omega - \int_\Sigma \mathcal{B} uv d\Sigma, \tag{4}$$

$$\ell(v) = \int_\Gamma gv \, d\Gamma. \tag{5}$$

In the simplest form, the low-order Robin boundary condition $\mathcal{B}u = -iku$ can be used to approximate the Sommerfeld's radiation condition. In the present paper, we analyze the BGT-2 and Karp's far-field expansion ABCs in 2D, the Wilcox's far-field expansion ABC in 3D, and compare the performance of FEM with IGA, both with and without eliminating domain truncation error.

2.1 2D BGT-2 ABC

The symmetrical second-order Bayliss-Gunzburger Turkel ABC (BGT-2) can be defined by using $\mathcal{B}u := \partial_s(\alpha \partial_s u) - \beta u$, and

$$\alpha := -\frac{1}{2ik(1 + i\kappa/k)} \ , \qquad \beta = -ik + \frac{\kappa}{2} - \frac{\kappa^2}{8(\kappa - ik)} \ , \tag{6}$$

where κ is the curvature over the surface Σ and the curvilinear derivative is ∂_s. The BGT-2 boundary condition can be written in the weak form

$$\begin{aligned}\int_\Sigma \mathcal{B}uvd\Sigma &= \int_\Sigma \partial_s^2(\alpha u)vd\Sigma - \int_\Sigma \beta uvd\Sigma = -\int_\Sigma \alpha\partial_s u\partial_s vd\Sigma - \int_\Sigma \beta uvd\Sigma \\ &= \int_\Sigma \frac{1}{2ik(1+i\kappa/k)}\partial_s u\partial_s vd\Sigma - \int_\Sigma \left(-ik + \frac{\kappa}{2} - \frac{\kappa^2}{8(\kappa - ik)}\right) uvd\Sigma.\end{aligned} \tag{7}$$

Hence, the bilinear form $a(u,v)$ is

$$\begin{aligned}a(u,v) = \int_\Omega \nabla u\cdot\nabla v - k^2uv\,d\Omega - \int_\Sigma \frac{1}{2ik(1+i\kappa/k)}\partial_s u\partial_s vd\Sigma \\ + \int_\Sigma \left(-ik + \frac{\kappa}{2} - \frac{\kappa^2}{8(\kappa - ik)}\right) uvd\Sigma.\end{aligned} \tag{8}$$

When the domain is truncated with a circular fictitious boundary Σ of radius R_1, the curvature is then $\kappa = 1/R_1$.

2.2 2D Karp's Far-field Expansion ABC

Let us fix a circular fictitious boundary Σ with radius R_1. We consider the Karp's expansion [49]. Its first- and second-order radial derivatives accompanied by recurrence equations require to determine two families of added auxiliary unknowns on the fictitious boundary Σ. In this case, $\mathcal{B}u$ can be obtained by using the radial derivative of the Karp's expansion. More precisely, let us introduce

$$u(R_1,\theta) = H_0(kR_1)\sum_{l=0}^{L-1}\frac{F_l(\theta)}{(kR_1)^l} + H_1(kR_1)\sum_{l=0}^{L-1}\frac{G_l(\theta)}{(kR_1)^l}, \tag{9}$$

$$\partial_r u(R_1,\theta) = \partial_r\left(H_0(kr)\sum_{l=0}^{L-1}\frac{F_l(\theta)}{(kr)^l} + H_1(kr)\sum_{l=0}^{L-1}\frac{G_l(\theta)}{(kr)^l}\right)\Big|_{r=R_1}, \tag{10}$$

$$\partial_r^2 u(R_1,\theta) = \partial_r^2\left(H_0(kr)\sum_{l=0}^{L-1}\frac{F_l(\theta)}{(kr)^l} + H_1(kr)\sum_{l=0}^{L-1}\frac{G_l(\theta)}{(kr)^l}\right)\Big|_{r=R_1}, \tag{11}$$

$$2lF_l(\theta) = -l^2G_{l-1}(\theta) - d_\theta^2 G_{l-1}(\theta), \qquad \text{for } l = 1,2,\ldots. \tag{12}$$

$$2lG_l(\theta) = (l-1)^2F_{l-1}(\theta) + d_\theta^2 F_{l-1}(\theta), \qquad \text{for } l = 1,2,\ldots \tag{13}$$

We define the following space

$$\mathscr{S} = H^1(\Omega)\times\underbrace{H^1(S_R)\times H^1(S_R)\cdots\times H^1(S_R)}_{2L\text{ times}},$$

to rewrite the form a to solve (3) as: find $(u, F_0, G_0\ldots F_{L-1}, G_{L-1}) \in \mathscr{S}$ with

$$a(u,v) = \int_\Omega \nabla u\cdot\nabla v - k^2uvd\Omega - \int_\Sigma A_l(kR_1)F_lvd\Sigma - \int_\Sigma B_l(kR_1)G_lvd\Sigma, \tag{14}$$

where

$$\begin{aligned}A_l(kR) &= -kH_1(kR_1) - \frac{klH_0(kR_1)}{kR_1}, \\ B_l(kR_1) &= \frac{-k(l+1)H_1(kR_1)}{kR_1} + kH_0(kR_1).\end{aligned}$$

We denote the number of degrees of freedom on the artificial boundary with m. We add $2m$ columns to include the Karp's expansion to the linear system by using

$$\int_\Sigma uvd\Sigma - \int_\Sigma \left(H_0(kR_1) \sum_{l=0}^{L-1} F_l \right) vd\Sigma - \int_\Sigma \left(H_1(kR_1) \sum_{l=0}^{L-1} G_l \right) vd\Sigma = 0. \tag{15}$$

Next, we write $2m$ additional rows to satisfy

$$\begin{aligned} &\int_\Sigma \left(\sum_{l=0}^{L-1} P_l(kR_1) F_l(\theta) + \sum_{l=0}^{L-1} Q_l(kR_1) G_l(\theta) \right) vd\Sigma \\ &- \int_\Sigma \left(H_0(kR_1) \sum_{l=0}^{L-1} \frac{F_l'(\theta)}{(kR_1)^l} + H_1(kR_1) \sum_{l=0}^{L-1} \frac{G_l'(\theta)}{(kR_1)^l} \right) v' d\Sigma = 0, \end{aligned} \tag{16}$$

where

$$\begin{aligned} P_l(kR_1) &= C_l(kR_1) + \frac{1}{R_1} A_l(kR_1) + k^2 H_0(kR_1), \\ Q_l(kR_1) &= D_l(kR_1) + \frac{1}{R} B_l(kR_1) + k^2 H_1(kR_1), \end{aligned}$$

and

$$\begin{aligned} C_l(kR_1) &= -k^2 \left[\left(1 - \frac{l(l+1)}{(kR_1)^2} \right) H_0(kR_1) - \frac{2l+1}{(kR_1)} H_1(kR_1) \right], \\ D_l(kR_1) &= k^2 \left[-\frac{(2l+1) H_0(kR_1)}{kR_1} + \left(-1 + \frac{(l+1)(l+2)}{(kR_1)^2} \right) H_1(kR_1) \right]. \end{aligned}$$

Finally, we add $2m(L-1)$ rows to incorporate the recurrence formulas, for $l = 1 \dots L-1$,

$$\int_\Sigma \left(2lG_l - (l-1)^2 F_{l-1} \right) v \, d\Sigma + R_1^2 \int_\Sigma F_{l-1}'(\theta) v' \, d\Sigma = 0, \tag{17}$$

and

$$\int_\Sigma \left(2lF_l + l^2 G_{l-1} \right) v \, d\Sigma + R_1^2 \int_\Sigma G_{l-1}'(\theta) v' \, d\Sigma = 0. \tag{18}$$

This procedure increases the size of the stiffness matrix by $2mL$ to simultaneously solve the unknowns introduced through the far-field expansion. We note that KFE-ABC requires the evaluation of the first derivative only, similarly to BGT-2. The matrix structure is discussed in detail in [54].

The far-field pattern can be obtained from the numerical solution of the scattered field at the artificial boundary Σ. The points on the boundary should be equidistant in order to compute the far-field pattern by using

$$f_0(\theta) = \sqrt{\frac{2}{\pi}} e^{-i\pi/4} \sum_{q=-m/2}^{m/2-1} b_q (-i)^q e^{iq\theta}, \tag{19}$$

where $b_q = c_q / H_q^{(1)}(kR)$, and $H_q^{(1)}$ is the Hankel's function of first-kind and order q. Also, we set $(c_q)_{q=-m/2,\cdots m/2-1}$, as the discrete Fourier transform vector of the numerical solution on the artificial boundary, u_Σ being interpolated at the points $(\theta_{j\Sigma}, u_{j\Sigma})$ on Σ, and

$$c_q = \frac{1}{m} \sum_{j=1}^{m-1} u_{j\Sigma} e^{-iq\theta_{j\Sigma}} \quad \text{for} \quad q = -m/2, \cdots m/2 - 1, \tag{20}$$

m being the (even) number of points on the artificial boundary Σ. The exact solution at the far-field is obtained from

$$P(\theta) = -\Big(\frac{2}{k\pi}\Big)^{1/2} e^{-i\pi/4} \sum_{n=0}^{\infty} \epsilon_n \frac{J_n^{'}(kR_0)}{H_n^{(1)}(kR_0)} \cos(n\theta), \tag{21}$$

where R_0 is the radius of a circular scatterer centered at origin and $J_n^{'}$ is the derivative of the Bessel's functions of the first-kind. The parameter ϵ_n is the Jacobi symbol: $\epsilon_0 = 0$, and $\epsilon_n = 2$ for $n = 1, 2, 3, ...$

2.3 3D Wilcox's Far-field Expansion ABC

The higher order absorbing boundary condition for the three-dimensional scattering problem can be given by the Wilcox's expansion. The sphere is of radius R_1 with surface $\Sigma := \mathbb{S}$. Let us introduce

$$u(R_1, \theta, \phi) = \frac{e^{ikR_1}}{(kR_1)} \sum_{l=0}^{L-1} \frac{F_l(\theta, \phi)}{(kR_1)^l}, \tag{22}$$

$$\partial_r u(R_1, \theta, \phi) = \frac{e^{ikR_1}}{(kR_1)^l} \left(\sum_{l=0}^{L-1} \left(ik - \frac{l+1}{R_1} \right) \frac{F_l(\theta, \phi)}{(kR_1)^l} \right) \Bigg|_{r=R_1}, \tag{23}$$

$$2ilF_l(\theta, \phi) = l(l-1)F_{l-1}(\theta, \phi) + \Delta_{\mathbb{S}} F_{l-1}(\theta, \phi). \tag{24}$$

The Wilcox's expansion has only one recurrence formula. Thus, only the radial derivative continuity equation is sufficient to define the boundary conditions. In the above expressions, $\Delta_{\mathbb{S}}$ is the Laplace-Beltrami operator in spherical coordinates.

We define

$$\mathscr{S} = H^1(\Omega) \times \underbrace{H^1(S_R) \times H^1(S_R) \cdots \times H^1(S_R)}_{L \text{ times}},$$

the bilinear form $a(u, v)$ involved in (3) is: find $(u, F_0, \ldots F_{L-1}) \in \mathscr{S}$ such that

$$a(u, v) = \int_{\Omega} \nabla u \cdot \nabla v - k^2 uv d\Omega - \frac{e^{ikR_1}}{(kR_1)^{l+1}} \left(ik - \frac{l+1}{R} \right) F_l v d\Sigma. \tag{25}$$

For m degrees of freedom on the artificial boundary, we add m equations to the linear system of equations based on

$$\int_{\Sigma} uv d\Sigma - \frac{e^{ikR_1}}{(kR_1)^{l+1}} F_l v d\Sigma, \tag{26}$$

and fix $m(L-1)$ rows for the recurrence formula, for $l = 1 \ldots L-1$, through

$$\int_{\Sigma} \left(-l(l-1)F_{l-1} \right) v \, d\Sigma + R_1^2 \int_{\Sigma} F_{l-1}'(\theta) v' \, d\Sigma = 0. \tag{27}$$

The implementation is similar to the KFE-ABC in 2D, but the Wilcox's expansion has only one recurrence formula.

3 Comparison between FEM and IGA with no domain truncation error

In this section, we study the performance of high-order FEM and compare it to IGA by solving two benchmark problems: (a) the propagation in an infinite waveguide along the x-axis and (b) the scattering by a sound-hard circular cylinder subject to an incident plane wave. By adopting modified exact solutions, the domain truncation error is removed. Therefore, the comparison performed in this section is an indicator of the performance of IGA and FEM in solving time-harmonic acoustic problem regardless of the ABC used to truncate the domain. For discussing the results, the relative L_2-error is employed

$$\epsilon_2 = \frac{\left\{ \int_\Omega |f^h(\mathbf{x}) - f^{\text{ex}}(\mathbf{x})|^2 d\mathbf{x} \right\}^{1/2}}{\left\{ \int_\Omega |f^{\text{ex}}(\mathbf{x})|^2 d\mathbf{x} \right\}^{1/2}}, \tag{28}$$

where f^h is the numerical solution and f^{ex} is the exact solution. Such comparison sheds light on the levels of the pollution error of each method and clarify the minimum error one can expect for a given refinement and frequency without domain truncation error.

3.1 Waveguide problem

In the first example, we analyze the case of an infinite waveguide along the x-axis. To compare the performance between FEM and IGA, we consider the truncated domain $\Omega = [0, 2] \times [0, 1]$ (see Fig. 1). We assume rigid lower and upper walls and denote the outward unit normal vector by $\mathbf{n}$. The domain is discretized with Lagrange and NURBS basis functions with order p, for a discretization density n_λ.

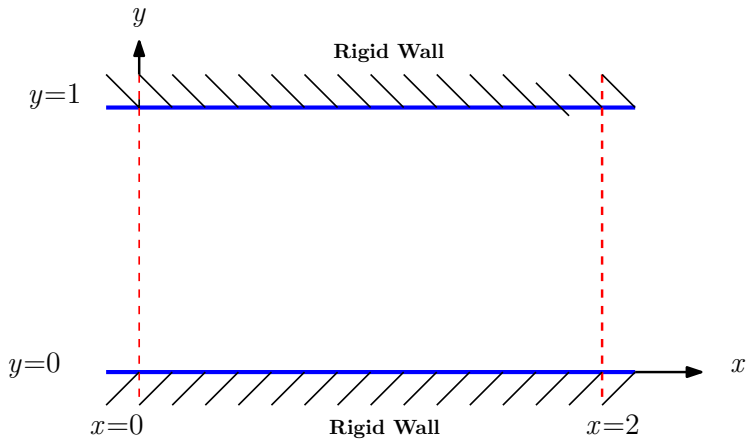

Figure 1: Waveguide along the x-axis.

We solve the Helmholtz problem to find the acoustic pressure u in the duct with the

following boundary conditions

$$\begin{aligned} &\Delta u + k^2 u = 0, && \text{in } \Omega^-, \\ &\partial_{\mathbf{n}} u = \cos(c\pi y), && \text{on } x = 0, \\ &\partial_{\mathbf{n}} u - \mathcal{B}u = 0, \ (\mathcal{B}u = -iku), && \text{on } x = 2, \\ &\partial_{\mathbf{n}} u = 0, && \text{on } y = 0, 1, \end{aligned} \tag{29}$$

where $c \in \mathbb{N}$ is the mode number. The inlet is subject to inhomogeneous Neumann boundary conditions and absorbing (and transparent for $c = 0$) boundary condition on the outlet boundary ($x = 2$). Since the boundaries at $y = 0, 1$ are assumed to be perfectly rigid, the normal derivative of the acoustic pressure vanishes on these boundaries. The exact solution of problem (29) with ABC is given as [59]

$$u^{\text{ex}}(x, y) = \cos(c\pi y)(A_1 e^{-ik_x x} + A_2 e^{ik_x x}), \tag{30}$$

where $k_x = \sqrt{k^2 - (c\pi)^2}$ and the coefficients A_1 and A_2 are obtained from

$$i \begin{pmatrix} k_x & -k_x \\ (k - k_x)e^{-2ik_x} & (k + k_x)e^{2ik_x} \end{pmatrix} \begin{pmatrix} A_1 \\ A_2 \end{pmatrix} = \begin{pmatrix} 1 \\ 0 \end{pmatrix}.$$

We get the expression of the modified exact solution by solving this 2×2 linear system. Since this is a modified exact solution, it does not capture the error introduced by applying the ABC on the duct outlet. This provides the possibility to study the finite-dimensional approximation regardless of the ABC applied. The duct cut-off frequency is $c_{\text{cut-off}} = k/\pi$. The wave propagation in the duct propagates when $c \leq c_{\text{cut-off}}$, and it represents evanescent modes when $c > c_{\text{cut-off}}$. The real parts of estimated FEM and IGA solutions for $k = 40$, $c = 2$, $p = 3$, $n_\lambda = 10$ are presented in Figs 2a and 2b respectively.

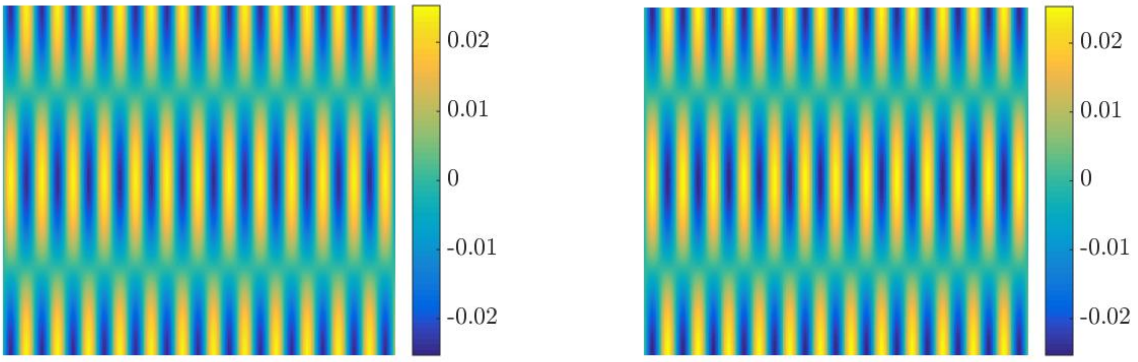

(a) $\Re(u_h)_{\text{FEM}}$ (b) $\Re(u_h)_{\text{IGA}}$

Figure 2: Real part of the numerical solution for $k = 40$, $p = 3$, $n_\lambda = 10$.

The corresponding absolute errors are compared in Figs 3a and 3b, respectively. The geometry is exactly represented in both cases, but the error obtained by using the IGA is about two orders lower than that of FEM. This could possibly be attributed to the smooth and higher order continuous NURBS basis functions.

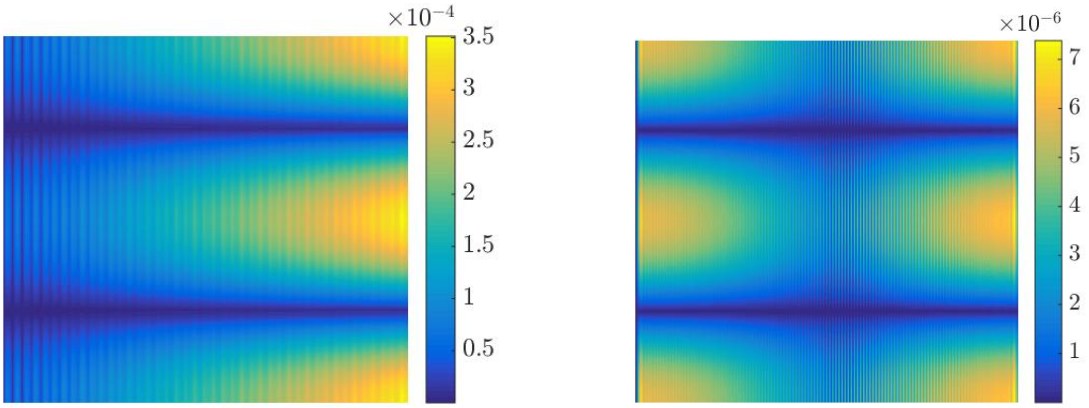

(a) $|u^{\text{ex}} - u_h|_{\text{FEM}}$ (b) $|u^{\text{ex}} - u_h|_{\text{IGA}}$

Figure 3: Absolute error $|u^{\text{ex}} - u_h|$ for $k = 40$, $p = 3$, $n_\lambda = 10$. The numerical error of IGA is considerably lower for the identical basis order, number of DOFs, and integration points even when there is no geometrical errors.

The evolution of the relative L_2-error with discretization density n_λ for the wave number $k = 40$ and according to the wave number k for $n_\lambda = 10$ are shown in Figs 4a-4b, respectively. In both cases, the mode number c is taken as 2. The results are shown for different orders of basis functions, $p = 1, \cdots, 5$. The slope of the graphs are noted with s in the legend. It is seen that the error of the FEM and the IGA are identical when $p = 1$, as expected. Indeed, the IGA basis functions are then not different from linear Lagrangian basis functions. It is evident that IGA yields more accurate results per DOF for a given basis order. For $p > 1$, the relative error in IGA decreases sharply, most particularly for $p \geq 3$. The increase in the error with respect to k is observed for both the Lagrange and IGA basis functions, when $p \leq 3$. This is an indicator of the pollution error. Interestingly, the pollution in IGA seems to be (almost) fully under control for orders $p \geq 3$ and a fixed discretization density n_λ. This could be attributed to the higher order and globally continuous basis functions employed in the IGA.

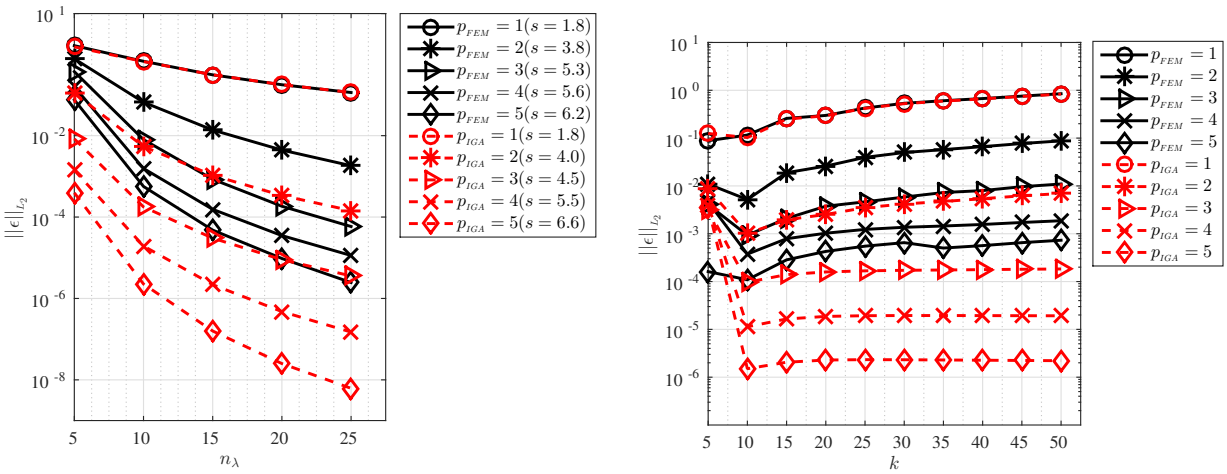

(a) (b)

Figure 4: Error evolution for $k = 40$ and $c = 2$, for $p = 1, \cdots, 5$.

3.2 Scattering by a sound-hard circular cylinder

We consider now the acoustic scattering of a circular cylinder with radius $R_0 = 1$ centered at the origin. The BGT-2 type boundary condition is applied on the fictitious circular boundary at radius $R_1 = 2$ centered at $(0, 0)$. We consider the Neumann boundary conditions at the scatterer boundary Γ. The BVP is then given by: find u satisfying

$$\begin{aligned} &\Delta u + k^2 u = 0, && \text{in } \Omega^-, \\ &\partial_{\mathbf{n}} u = g := -\partial_{\mathbf{n}} u^{\text{inc}}, && \text{on } \Gamma(R_0 = 1), \\ &\partial_{\mathbf{n}} u - \mathcal{B} u = 0, && \text{on } \Sigma(R_1 = 2). \end{aligned} \tag{31}$$

We apply the BGT-2 boundary condition on the fictitious boundary Σ following the weak form developed in Section 2.1 and consider an incident plane wave $u^{\text{inc}}(\mathbf{x}) = e^{ik\mathbf{d}\cdot\mathbf{x}}$, where $\mathbf{d}$ is the incidence direction $\mathbf{d} = (\cos(\theta^{\text{inc}}), \sin(\theta^{\text{inc}}))^T$ and θ^{inc} is the scattering angle. Since this problem is symmetric, we can fix the incidence direction to $\mathbf{d} = (1, 0)^T$. The modified exact solution can be obtained as a summation of modal solutions [25]

$$u^{\text{ex}} = \sum_{m\in\mathbb{Z}} i^m u_m^{\text{ex}}, \tag{32}$$

where

$$u_m^{\text{ex}}(\mathbf{x}) = \left(a_m H_m^{(1)}(kr) + b_m H_m^{(2)}(kr)\right) e^{im\phi}, \quad R_1 \geq r \geq R_0, \quad m \in \mathbb{Z}. \tag{33}$$

Here, $H_m^{(1)}$ and $H_m^{(2)}$ are the m^{th} order first- and second-kind Hankel functions, respectively. The Neumann boundary condition is applied at the scatterer boundary Γ at R_0 and the ABC is applied on the fictitious boundary Σ at R_1. This results in the linear system of equations with two unknowns a_m and b_m.

$$a_m = -\frac{A_{22}^m J_m'(kR_0)}{D_m}, \quad b_m = \frac{A_{21}^m J_m'(kR_0)}{D_m}, \tag{34}$$

where $D_m = A_{11}^m A_{22}^m - A_{21}^m A_{12}^m$ and

$$\begin{cases} A_{11}^m = H_m'^{(1)}(kR_0), & A_{21}^m = kH_m'^{(1)}(kR_1) - \mathcal{B}_m H_m^{(1)}(kR_1), \\ A_{12}^m = H_m'^{(2)}(kR_0), & A_{22}^m = kH_m'^{(2)}(kR_1) - \mathcal{B}_m H_m^{(2)}(kR_1), \\ \mathcal{B}_m = -\left(\alpha_m \dfrac{m^2}{R_1^2} + \beta_m\right), & \alpha_m = -\dfrac{1}{2ik}\left(1 + \dfrac{i}{kR_1}\right)^{-1}, \\ \beta_m = -ik + \dfrac{1}{2R_1} + \dfrac{1}{8iR_1(i + kR_1)}. \end{cases}$$

We plot the real part of the numerical solutions obtained with FEM and IGA for $k = 40$, $p = 3$, $n_\lambda = 10$ in Figs 5a-5b, respectively. The corresponding absolute errors are also plotted in Fig. 6a for FEM, and Fig. 6b for IGA. The average absolute error obtained for FEM and IGA are in the range of 5×10^{-3} and 1.5×10^{-4}, respectively. Thus, the wave field is properly estimated over the domain considering its frequency and selected discretization density. Equal number of degrees of freedom ($397\times$ 64) were used for both FEM and IGA. The error of IGA is considerably lower which is consistent with the results obtained in Section 3.1. This is an indicator that IGA shape functions can conform better to the high oscillatory nature of the solution. The evolution of the relative L_2-error with

discretization density n_λ in FEM and IGA is shown in Fig. 7 for $k = 40$, $p = 1, \cdots, 5$. Both FEM and IGA meshes are structured and an identical number of radial and circumferential degrees of freedom were used in both methods. It is clear that IGA yields much higher accuracy per DOF for a given basis order and discretization density. The error levels shown in Fig. 8 are the minimum we can expect for the given wave number, basis order and discretization density regardless of the ABC applied to truncate the computational domain. This yields an improved computational cost when using IGA since an equivalent accuracy can be achieved with lower refinement.

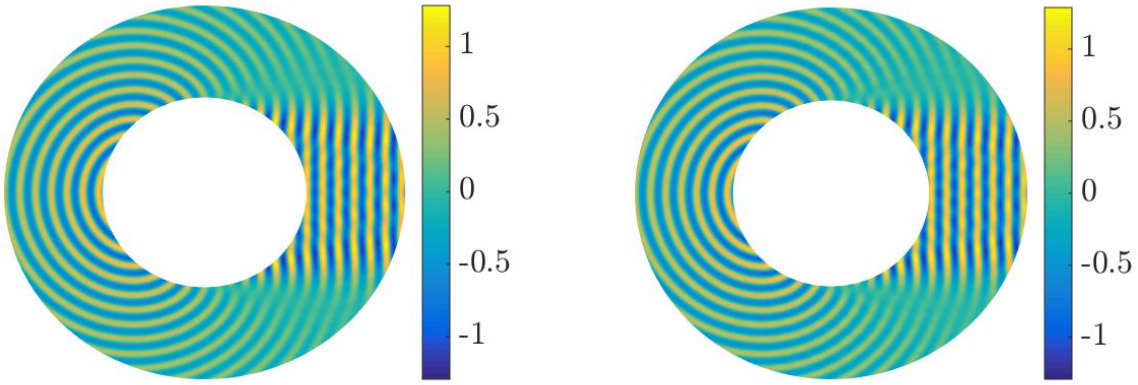

(a) $\Re(u_h)_{\text{FEM}}$ (b) $\Re(u_h)_{\text{IGA}}$

Figure 5: Real part of the numerical solution for $k = 40$, $p = 3$, $n_\lambda = 10$. The numerical solution in both FEM and IGA captures high oscillatory wave field.

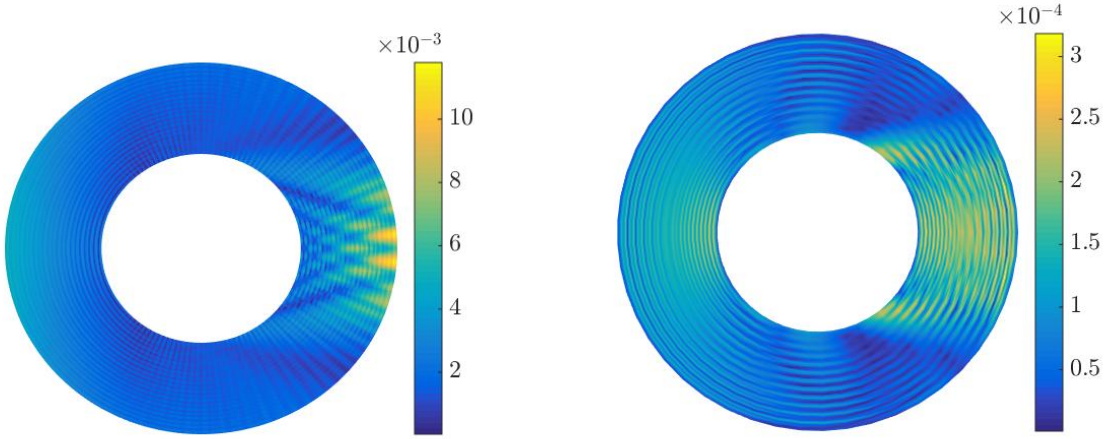

(a) $|u^{\text{ex}} - u_h|_{\text{FEM}}$ (b) $|u^{\text{ex}} - u_h|_{\text{IGA}}$

Figure 6: Absolute error $|u^{\text{ex}} - u_h|$ for $k = 40$, $p = 3$, $n_\lambda = 10$. The numerical error with IGA is considerably lower for the identical basis order, number of degrees of freedom and the integration points. The contribution of the domain truncation error was eliminated by considering BGT-2 type ABC and modified exact solution.

The evolution of the relative L_2-error with wave number k is shown in Fig. 8, for $p = 1, \cdots, 5$. Again, the BGT-2 type ABC is applied on the fictitious boundary at $R_1 = 2$ and

the contribution of the domain truncation error is eliminated from the error calculation by adopting the modified exact solution given in (33). Here, we can clearly see the advantage of IGA over FEM in solving high-frequency problems. The pollution error of IGA is really lower than that of FEM for the same order p and same number of degrees of freedom, providing excellent accuracy in mid- to high-frequencies. The low pollution error of IGA was also observed in [25] for very high frequencies but was not compared to the pollution error in FEM before.

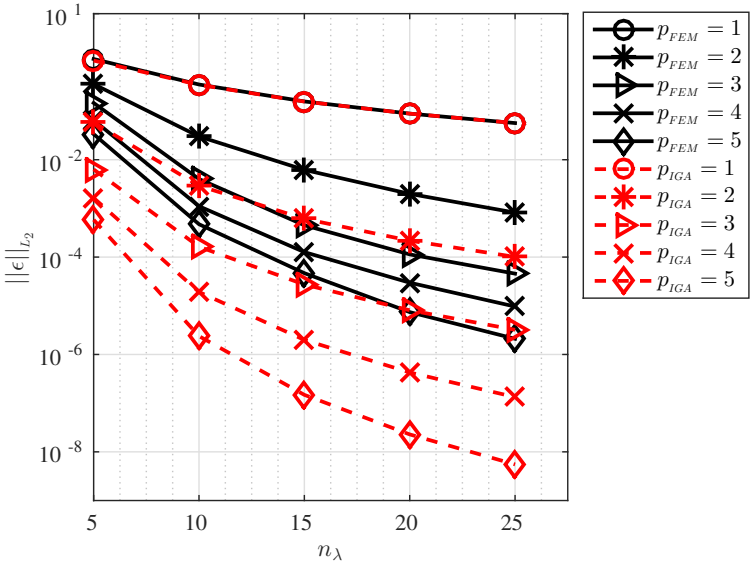

Figure 7: Evolution of relative L_2-error with n_λ for $k = 40$ for $p = 1, \cdots, 5$. The BGT-2 type ABC is applied on the fictitious boundary and a modified exact solution is used to evaluate the error.

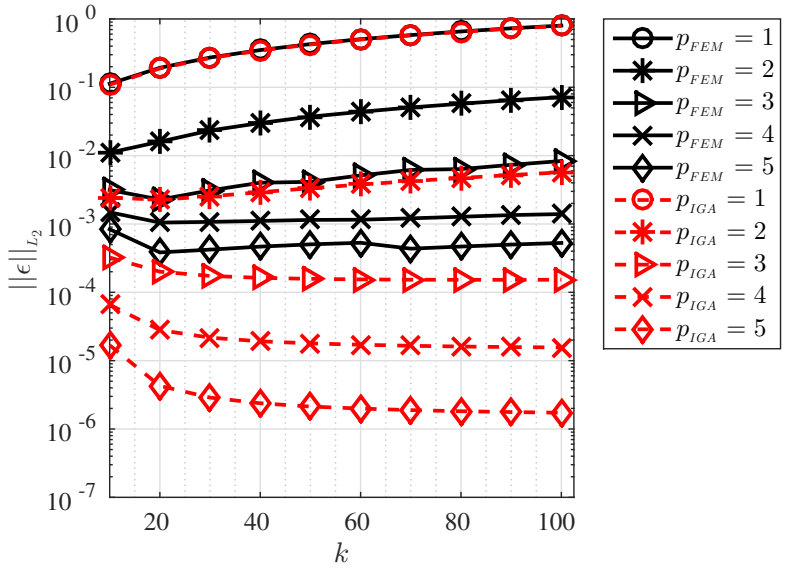

Figure 8: Relative error in L_2-norm, for $p = 1 \cdots, 5$ and $n_\lambda = 10$.

4 2D acoustic scattering with KFE-ABC: from low- to high- frequencies

In this section, we solve the acoustic scattering from a circular cylinder problem again after applying now the Karp's farfield expansion boundary condition on the fictitious boundary Σ. The boundary value problem reads:

$$\begin{aligned} &\Delta u + k^2 u = 0, && \text{in } \Omega^-, \\ &\partial_{\mathbf{n}} u = \partial_{\mathbf{n}} u^{\text{inc}}, && \text{on } \Gamma(R_0 = 1), \\ &\partial_{\mathbf{n}_\Sigma} u - \mathcal{B} u = 0, && \text{on } \Sigma(R_1 = 2). \end{aligned} \tag{35}$$

We adopt the weak form for KFE developed in Section 2.2, where $\mathcal{B}$ is a compact notation for representing the KPE ABC. The parameter NT denotes the number L of terms of the Karp's expansion. We compare the performance of FEM and IGA in the very low-, mid- and high-frequency regimes. First, we consider the wave number $k = 5$ and compute the far-field pattern from the numerical solution of the scattered field by using (19). We calculate the relative L_2-error in the far-field with the exact solution (21).

The evolution of the relative L^2-error in the computational domain and the far-field with discretization density n_λ and the number of Karp's expansion terms (NT) are compared in Figs 9a-9b, respectively, for both the FEM and IGA. The comparison is done for a wave number $k = 5$ and for the basis order $p = 5$. Unlike the analysis performed with the modified exact solution, the relative error of the FEM and the IGA are not significantly different for the selected range of the discretization density and the number of Karp's expansion terms. This is a clear indicator that for $k = 5$ and basis order $p = 5$, the ABC error is dominating the numerical solution for $NT \leq 7$. Moreover, with IGA, higher accuracy can be achieved by adding more terms in the KFE-ABC such that the accuracy matches that of the interior domain.

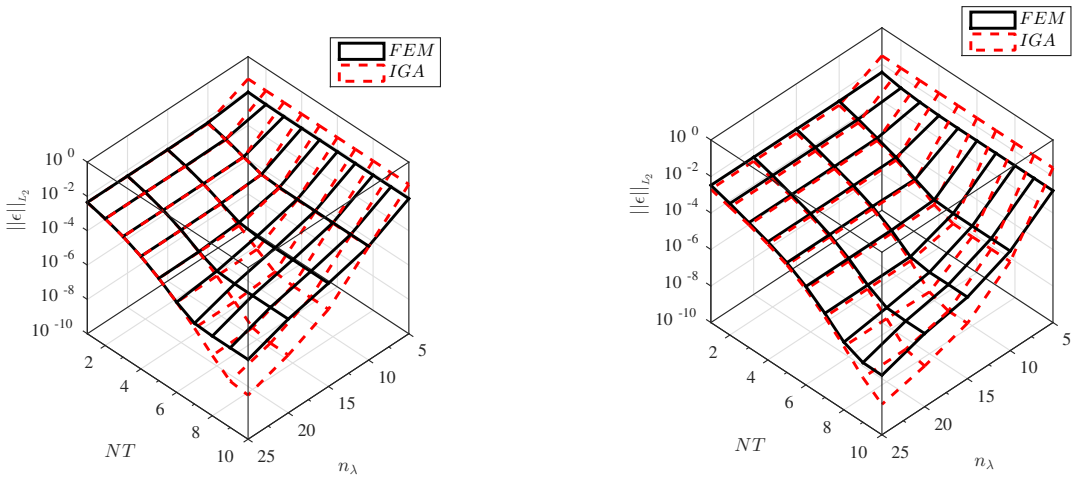

(a) Relative L_2-norm error in the interior

(b) Relative L_2-norm error in the far-field

Figure 9: Evolution of the relative L_2-error in the domain with discretization density n_λ and number of terms NT in Karp's expansion for $k = 5$, and basis order $p = 5$. By increasing NT, it is possible to match the higher accuracy of the IGA in the interior.

Next, we compare the relative error in L_2-norm of FEM and IGA in the interior domain for $k = 10$ and p =5, with varying discretization density n_λ and number of Karp's

expansion terms in Fig. 10. It is evident that the error obtained using IGA is smaller compared to FEM. As expected, the optimal number of Karp's expansion terms NT required depends on the accuracy of the numerical method in the interior. Therefore, it is a function of the wave number k, basis order p and discretization density n_λ. This can be confirmed by observing the optimal number of terms required in the FEM and IGA in Fig. 10. For the discretization density $n_\lambda = 5$, we see that the accuracy is not improved even after adding more terms. This is true for both methods and can be attributed to the coarse discretization in the interior.

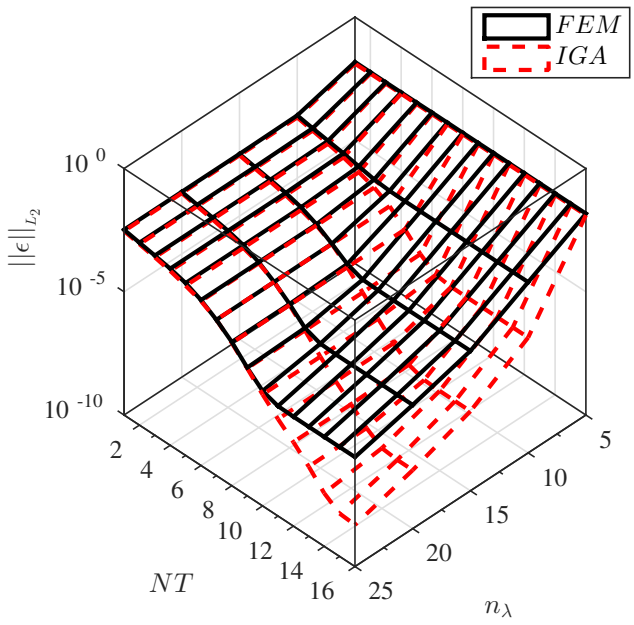

Figure 10: Relative error in L^2-norm for $p = 5$ and $k = 10$.

However, increasing the discretization density n_λ improves the accuracy of the FEM and IGA in the interior which should be matched by adding more ABC terms. With higher discretization densities, such as $n_\lambda = 25$, we remark a similar convergence for both the methods up to a certain number of Karp's expansion terms ($NT = 10$). Beyond, adding more terms only increases the accuracy in IGA but not in the FEM. The accuracy on the ABC is matching the accuracy of the FEM but not the IGA at $NT = 10$ and $n_\lambda = 25$. As a result, the IGA error is still dominated by the ABC. Hence, increasing the number of Karp's expansion terms to $NT = 20$ consistently reduces the error in the IGA. The continuity of the NURBS basis function used in this study is C^{p-1}, where p is the order of the basis function. If we keep the number of elements fixed and reduce the continuity to C^0, then the total number of degrees of freedom will increase to reduce the continuity which is sub-optimal. The discretization density n_λ in this study is defined based on the number of degrees of freedom as a fair basis for comparison. Let us consider a mesh with 37×10 degrees of freedom of order $p = 5$ in IGA which is C^4 continuous corresponding to a mesh made of 120 (20×6) meshes as shown in Fig. 11.

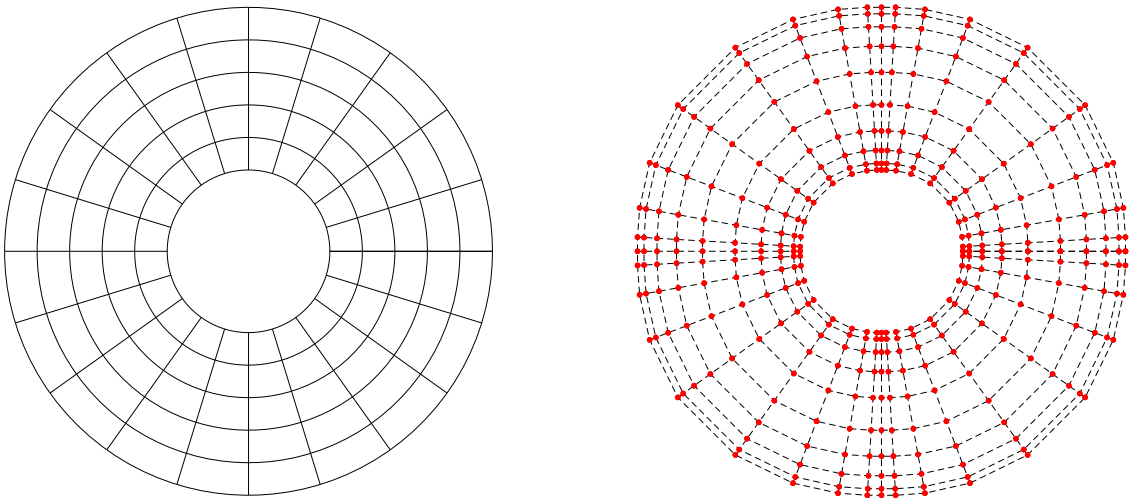

(a) IGA mesh (b) Location of degrees of freedom

Figure 11: (a) the mesh and (b) location of degrees of freedom of an analysis performed using $p = 5$, C^4 basis.

The number of meshes should be reduced to 24 (8×3) to maintain the number of degrees of freedom and reduce the continuity to C^0 in IGA. This reduction in number of meshes to maintain 120 degrees of freedom is shown in Fig. 12.

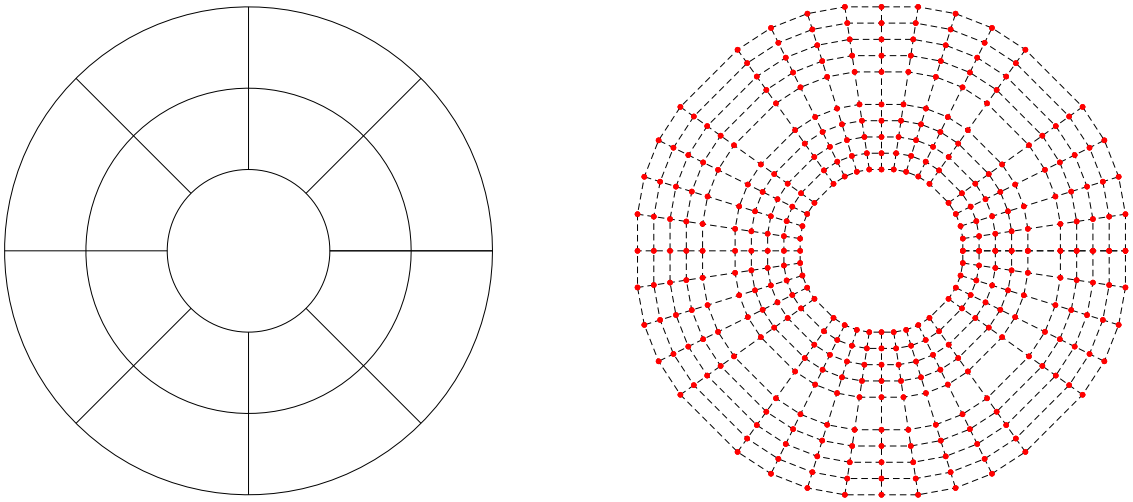

(a) IGA mesh (b) Location of degrees of freedom

Figure 12: (a) the mesh and (b) location of degrees of freedom of an analysis performed using $p = 5$, C^0 basis.

In order to better understand the effect of reducing the continuity in IGA, we plot in Fig. 13 the relative L^2-norm error calculated on the fictitious boundary for $k = 10$, $p = 5$, maintaining fixed the number of degrees of freedom for both the C^4 and C^0 analyses.

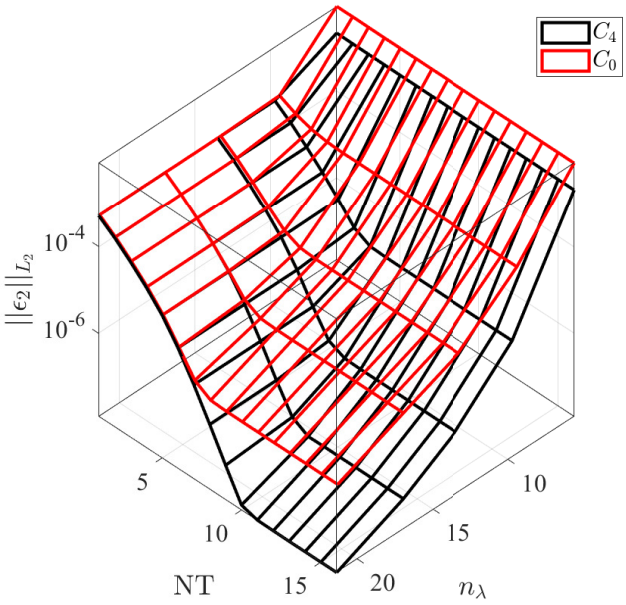

Figure 13: Relative L_2-norm error on the fictitious boundary for the C^4 and C^0 analyses. The accuracy is reduced by decreasing the continuity.

The evolution of the relative L_2-error in the interior domain with wave number k in the FEM is depicted in Fig. 14a when BGT-2 ABC is imposed on the artificial boundary. This is compared with only one Karp's expansion term $NT = 1$ in Fig. 14a, where $n_\lambda = 10$ and $p = 1, \cdots, 5$. For the low- to mid-frequency range, the BGT-2 and Karp's expansion with one term $NT = 1$ can be considered as equivalent. However, we note that BGT-2 or $NT = 1$ are not accurate enough for high-order FEM analysis. In order to find the minimum possible error achievable by increasing the number of Karp's expansion terms, we plot the evolution of the relative L_2-error in the interior domain by using the modified exact solution in Fig. 14b. It is clear that NT =1 is providing an adequate accuracy for $p = 1, 2, 3$ since the error calculated with the modified exact solution is not lower for $p \leq 3$. However, when using a basis order $p \geq 4$, the accuracy in the interior is increased beyond BGT-2 and $NT = 1$ accuracy and only one term of Karp's expansion is no longer enough. Hence, the error is dominated by the ABC error and we see that the error stagnates for $p \geq 4$ in Fig. 14b.

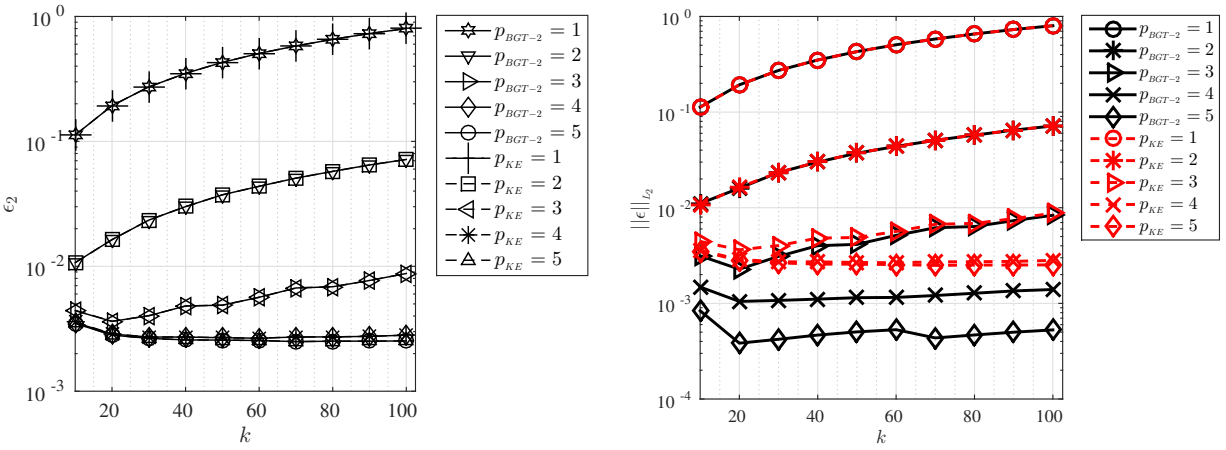

(a) BGT-2 is equivalent to KFE for $NT = 1$ (b) Domain truncation error

Figure 14: Comparison of BGT-2 and KFE ABCs with a single term in mid- to high-frequency regime and the minimum relative L_2-error in the interior domain for $p = 1, \cdots, 5$, $k = 10, \cdots, 100$ and $n_\lambda = 10$. More ABC terms should be added to match the accuracy of the interior solution when $p \geq 4$.

The proposed boundary condition is now applied to the boundary $R_1 = 1.05$. The radius of the scatterer is still $R_0 = 1$. This makes the domain of interest in which the computations are required very small, thus decreasing the computational effort enormously. Fig. 15 shows the error obtained for FEM and IGA for $p = 5$, $k = 5$, $NT = 25$ and $R_1 = 1.05$. For the same discretization density and number of terms, the accuracy of IGA is higher than for FEM.

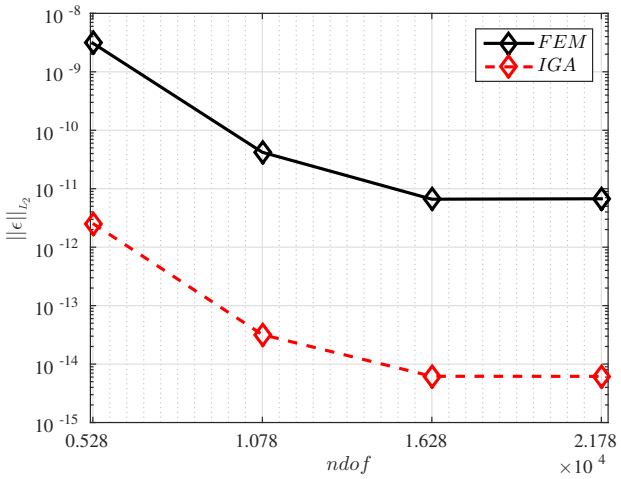

Figure 15: Relative L_2-error for the artificial boundary truncated at 5% increase in radius compared to the scatterer radius.

Since IGA is more precise than FEM, we now only retain IGA for the simulations. The advantage of Karp's ABC over BGT-2 to truncate the computational domain close to the boundary of the scatterer is demonstrated in Fig. 16, where $R_1 = 1.2$, enclosing the unit circular cylinder with $R_0 = 1$. The increased truncation radius from $R_1 = 1.05$ in Fig. 15 to $R_1 = 1.2$ in Fig. 16 allows a large enough computational domain for comparing

the absolute error obtained by using BGT-2 with the one obtained with Karp's expansion ABC. An incident plane wave for $k = 10$ was considered and the numerical results were found by using the basis order $p = 5$ and $n_\lambda = 12$. A considerable improvement is observed by switching to Karp's ABC. We note that the fictitious boundary R_1 can be considered very close to the scattering surface, leading to a highly reduced computational cost and an accurate solution.

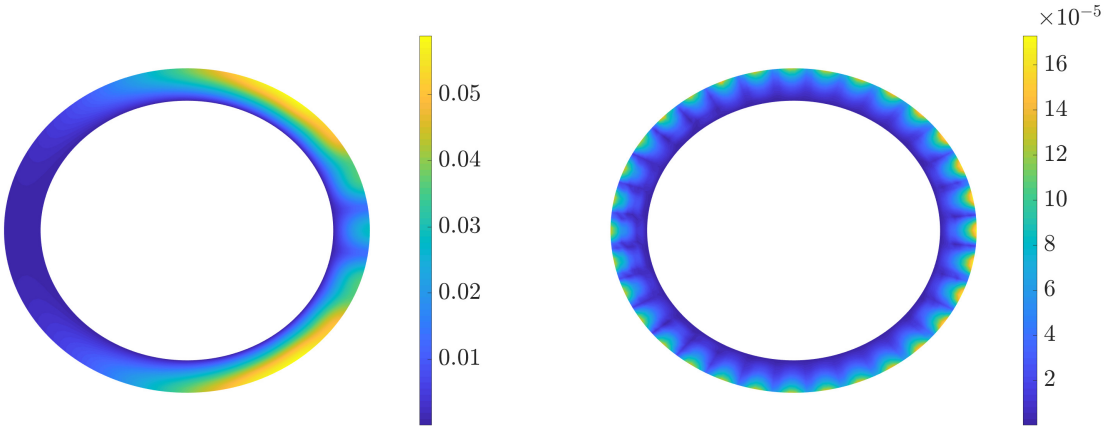

(a) BGT-2 (b) Karp's Expansion with $NT = 20$

Figure 16: Absolute error with $R_1 = 1.2$, $k = 10$, $p = 5$.

Let us apply the BGT-2 and KFE-ABC to the circular boundary at $R_1 = 2$, enclosing a 2D submarine-like shape. We consider the wave number $k = 50$ and an incident plane wave. We truncate the domain at $R_1 = 2$ and $R_1 = 1.5$, without changing the discretization density. The estimated total field is shown in Fig. 17 ($R_1 = 2$) and Fig. 18 ($R_1 = 1.5$) for the IGA basis order $p = 5$, and five terms in the Karp's expansion, i.e. $NT = 5$. Reducing the size of the computational domain yields less degrees of freedom. More precisely, the number of DOFs is reduced by 30%, passing from 25600 (320×80) to 17920 (320×56). We note that this reduction can be more significant for scatterers of smaller slenderness ratio since the truncation boundary can be placed very close to the boundary of the scatterer. Getting Karp-like ABCs would be probably extremely efficient, most particularly for an IGA implementation.

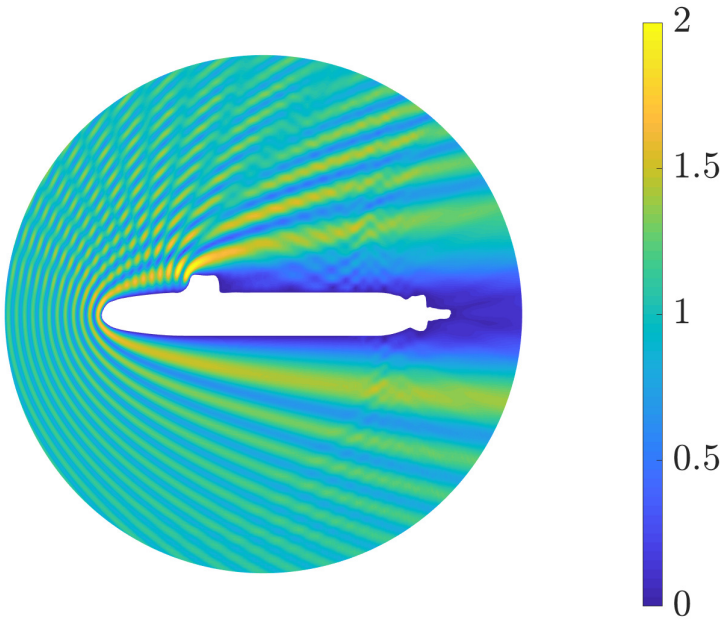

Figure 17: Total wave field scattered by a 2D submarine with a KFE-ABC set on a circular fictitious boundary with $R_1 = 2$

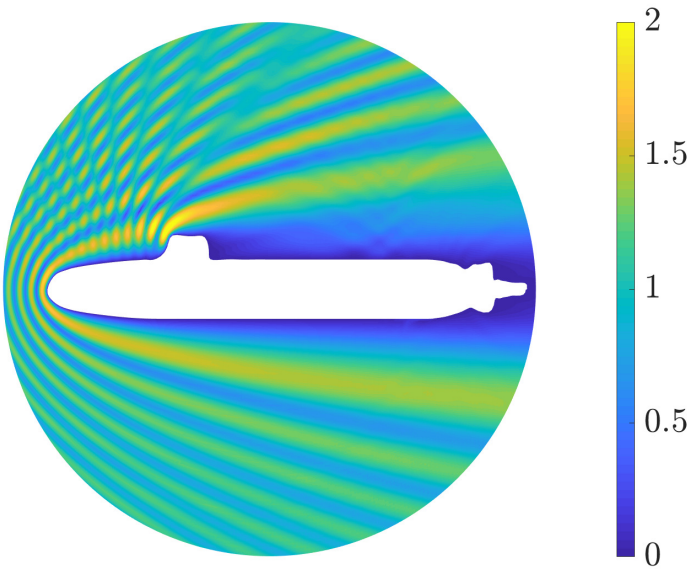

Figure 18: Total wave field scattered by a 2D submarine with a KFE-ABC set on a circular fictitious boundary with $R_1 = 1.5$.

5 3D acoustic scattering: numerical examples with IGA and WFE-ABC

To end, we now report some preliminary examples of simulations for 3D sound-soft obstacles. The frequency range studied here is not too high since the problems lead to very large size linear systems to resolve, needing some specifically designed DDM solvers. In addition, we only report results related to IGA which has been proved to be more accurate than FEM in 2D as well as for the WFE-ABC which is the extension to 3D of the accurate KFE-ABC.

To start, we plot the real part of the scattered field around the sound-soft sphere in Fig. 19 ($R_0 = 1$), for $p = 2$ and $n_\lambda = 6$ (16530 degrees of freedom), where we choose the mid-frequency $k = 10$. We retain $NT = 10$ terms in the Wilcox's expansion set on a spherical boundary of radius $R_1 = 2$.

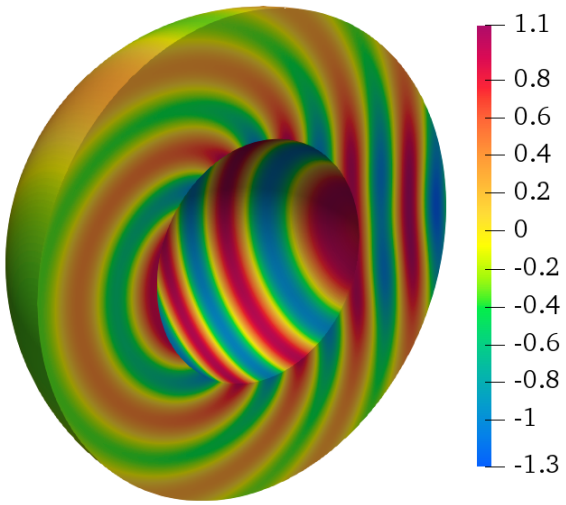

Figure 19: Real part of the scattered field produced by a sound-soft spherical scatterer of radius $R_1 = 1$, for $p = 5$ and 16530 degrees of freedom. The number of terms for the WPE-ABC is set to $NT = 10$. The wave number is $k = 10$.

Next, we demonstrate in Fig. 20 the effect of choosing the basis order and the need to increase the accuracy of the ABC by adding more terms in the Wilcox's expansion, for the wave number $k = 2\pi$. We observe that, for $p = 1$, the accuracy of IGA is rather low for the discretization densities $n_\lambda = 4 \cdots 10$. Therefore, implementing a more accurate ABC by increasing the number of terms in the Wilcox's expansion does not reduce the error. On the other hand, when the basis order $p = 4$ is used, IGA is much more accurate in the computational domain for the same discretization density. This improved accuracy is limited by the error related to the ABC employed. The error is not considerably reduced by increasing the basis order when $n_\lambda = 10$, and $NT = 1$. This shows that the error of the high order analysis is bounded by that of the ABC. However, by adding more terms in the Wilcox's expansion, the error reduces to the minimal IGA accuracy for the selected basis order and discretization density, thus effectively avoiding the domain truncation error.

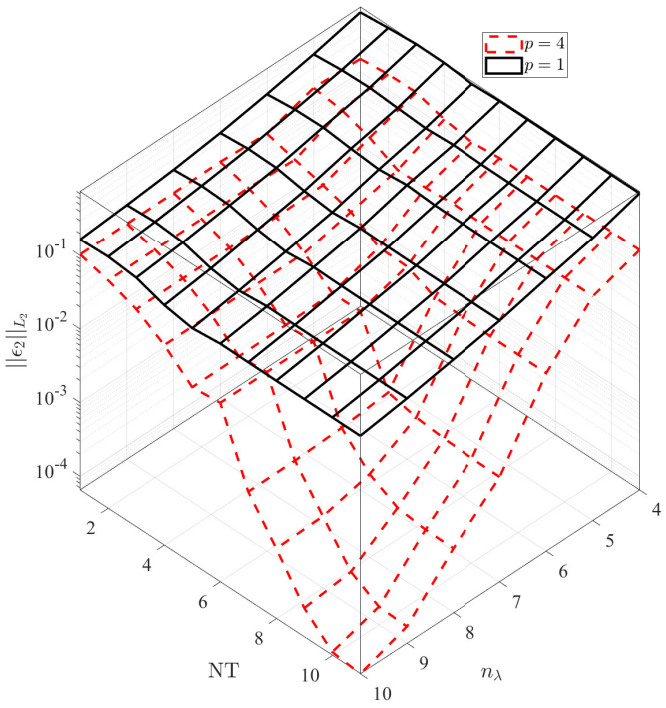

Figure 20: Relative L_2-norm error according to the discretization density n_λ and number of terms NT in the Wilcox's expansion for the scattering problem by the unit sphere.

The real part of the scattered field by a sound-soft ellipsoid with semi-axes 1.5, 0.5 and 0.5, along the x-, y- and z-directions, respectively, is shown in Fig. 21. The incident plane wave has a wave number $k = 10$. The analysis was performed by IGA with basis order $p = 5$, for 16530 degrees of freedom. The number of terms of the WFE-ABC is equal to $NT = 10$. This shows that the scattering for a complex geometry can also be studied by using the high-order WFE-ABC with IGA. However, more investigations still remain to be performed to confirm this general behavior. In addition, it would be extremely interesting, similarly to the 2D submarine case, to derive WPE-ABCs for a spheroidal fictitious boundary since this would lead to the possibility of diminishing the number of DOFs and then to better prospect high-frequency wave scattering. Finally, the full 3D methodology still needs to be investigated with more details concerning many aspects: convergence rate for complex problems, conditioning and spectral distribution related to the matrix defining the linear system,... However, this is out of the scope of the present paper.

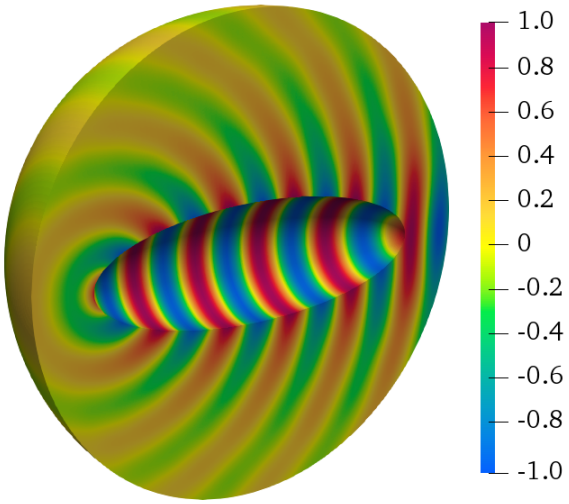

Figure 21: Real part of the scattered field produced by an ellipsoid using $p = 5$ and $n_\lambda = 6$ for IGA. The number of terms for the WPE-ABC is set to $NT = 10$. The wave number is $k = 10$.

6 Conclusions

The performance of high order FEM and IGA in solving exterior acoustic scattering problems was systematically studied and 3D numerical simulations were reported to illustrate the extension of the proposed method. First, the domain truncation error was artificially removed by applying the BGT-2 absorbing boundary condition on the fictitious boundary and then modifying the exact solution. Compared with FEM, the numerical results showed that the IGA yields higher accuracy per degree of freedom and suffers less from pollution for a given basis order and discretization density regardless of the method used to truncate the domain. Hence, one can expect a lower numerical error when using IGA if the error introduced by the domain truncation is not dominant. Next, KFE- and WFE-ABCs were applied in both IGA and FEM, for 2D and 3D problems, respectively. The evolution of the error was studied with h- and p-refinements. In addition, the number of ABC terms is also analyzed. Again, it was shown that higher order IGA can achieve superior accuracy per degrees of freedom when compared with the conventional FEM. It is opined that the error introduced by ABC can be conveniently reduced to match the accuracy of the higher order method employed in the interior domain. Therefore, it is possible to reduce the numerical error to fully eliminate the effect of the domain truncation by increasing the number of ABC terms.

References

[1] G. Seriani. 3-D spectral element-by-element wave modelling on Cray T3E. *Physics and Chemistry of the Earth, Part A: Solid Earth and Geodesy*, 24(3):241–245, 1999.

[2] W. Dauksher and A.F. Emery. Accuracy in modeling the acoustic wave equation with Chebyshev spectral finite elements. *Finite Elements in Analysis and Design*, 26(2):115–128, 1997.

[3] W. Dauksher and A.F. Emery. The solution of elastostatic and elastodynamic problems with Chebyshev spectral finite elements. *Computer Methods in Applied Mechanics and Engineering*, 188(1-3):217–233, 2000.

[4] C. Willberg, S. Duczek, J.M. Vivar-Perez, and Z.A.B. Ahmad. Simulation methods for guided wave-based structural health monitoring: a review. *Applied Mechanics Reviews*, 67(1):010803, 2015.

[5] A. Marzani, E. Viola, I. Bartoli, F.L. Di Scalea, and P. Rizzo. A semi-analytical finite element formulation for modeling stress wave propagation in axisymmetric damped waveguides. *Journal of Sound and Vibration*, 318(3):488–505, 2008.

[6] Z.A.B. Ahmad and U. Gabbert. Simulation of lamb wave reflections at plate edges using the semi-analytical finite element method. *Ultrasonics*, 52(7):815–820, 2012.

[7] Z.A.B. Ahmad, J.M. Vivar-Perez, and U. Gabbert. Semi-analytical finite element method for modeling of lamb wave propagation. *CEAS Aeronautical Journal*, 4(1):21–33, 2013.

[8] L.L. Thompson. A review of finite-element methods for time-harmonic acoustics. *The Journal of the Acoustical Society of America*, 119(3):1315–1330, 2006.

[9] Y. Saad. *Iterative methods for sparse linear systems*. 2nd ed., Society for Industrial and Applied Mathematics, Philadelphia, 2003.

[10] X. Antoine and M. Darbas. Alternative integral equations for the iterative solution of acoustic scattering problems. *Quaterly Journal of Mechanics and Applied Mathematics*, 58(1):107–128, 2005.

[11] X. Antoine and M. Darbas. Generalized combined field integral equations for the iterative solution of the three-dimensional Helmholtz equation. *ESAIM-Mathematical Modelling and Numerical Analysis*, 41(1):147–167, 2007.

[12] M. Darbas, E. Darrigrand, and Y. Lafranche. Generalized combined field integral equations for the iterative solution of the three-dimensional Helmholtz equation. *Journal of Computational Physics*, 236:289–316, 2013.

[13] K. Vater, T. Betcke, and B. Dilba. Simple and efficient GPU parallelization of existing H-Matrix accelerated BEM code. *arXiv preprint arXiv:1711.01897*.

[14] A. Lieu, G. Gabard, and H. Beriot. A comparison of high-order polynomial and wave-based methods for Helmholtz problems. *Journal of Computational Physics*, 321:105–125, 2016.

[15] G. Ernst and M.J. Gander. Why it is difficult to solve Helmholtz problems with classical iterative methods. *Numerical Analysis of Multiscale Problems*, pages 325–363, 2012.

[16] Y. Boubendir, X. Antoine, and C. Geuzaine. A quasi-optimal non-overlapping domain decomposition algorithm for the Helmholtz equation. *Journal of Computational Physics*, pages 262–280, 2012.

[17] L. Lehmann, S. Langer, and D. Clasen. Scaled boundary finite element method for acoustics. *Journal of Computational Acoustics*, 14(4):489 – 506, 2006.

[18] L. Liu, J. Zhang, C. Song, C. Birk, and W. Gao. An automatic approach for the acoustic analysis of three-dimensional bounded and unbounded domains by scaled boundary finite element method. *International Journal of Mechanical Sciences*, 151:563 – 581, 2019.

[19] C. Marot, J. Pellerin, and J.-F. Remacle. One machine, one minute, three billion tetrahedra. *International Journal for Numerical Methods in Engineering*, 117(9):967–990, 2019.

[20] E. Cohen, T. Martin, R.M. Kirby, T. Lyche, and R.F. Riesenfeld. Analysis-aware modeling: Understanding quality considerations in modeling for isogeometric analysis. *Computer Methods in Applied Mechanics and Engineering*, 199(5-8):334–356, 2010.

[21] T.J.R. Hughes, J.A. Cottrell, and Y. Bazilevs. Isogeometric analysis: CAD, finite elements, NURBS, exact geometry and mesh refinement. *Computer Methods in Applied Mechanics and Engineering*, 194(39-41):4135–4195, 2005.

[22] X. Gang, L. Bojian, S. Laixin, C. Long, X. Jinlan, and T. Khajah. Efficient r-adaptive isogeometric analysis with winslow's mapping and monitor function approach. *Journal of Computational and Applied Mathematics*, 351:186 – 197, 2019.

[23] G. Dodgen and T. Khajah. Effectiveness of Tikhonov Smoothing in isogeometric shape optimization of the horn speaker. *ASEE-GSW*, 2019.

[24] V. K. Ummidivarapua, H. K. Vorugantia, T. Khajah, and S. P. A. Bordas. Isogeometric shape optimization using Teaching Learning-Based Optimization (TLBO) algorithm. *Submitted - Computer Aided Geometric Design*, 351:186 – 197, 2019.

[25] T. Khajah, X. Antoine, and S.P.A. Bordas. B-spline FEM for time-harmonic acoustic scattering and propagation. *Journal of Theoretical and Computational Acoustics*, 27(3):1850059, 2019.

[26] J. Videla, C. Anitescu, T. Khajah, S.P.A. Bordas, and E. Atroshchenko. h- and p-adaptivity driven by recovery and residual-based error estimators for PHT-splines applied to time-harmonic acoustics, 2019.

[27] J.A. Cottrell, A. Reali, Y. Bazilevs, and T.J.R. Hughes. Isogeometric analysis of structural vibrations. *Computer Methods in Applied Mechanics and Engineering*, 195(41-43):5257–5296, 2006.

[28] J.-P. Bérenger. A perfectly matched layer for the absorption of electromagnetic waves. *Journal of Computational Physics*, 114(2):185–200, 1994.

[29] J.-P. Bérenger. Three-dimensional perfectly matched layer for the absorption of electromagnetic waves. *Journal of Computational Physics*, 127(2):363–379, 1996.

[30] A. Bermúdez, L. Hervella-Nieto, A. Prieto, and R. Rodríguez. An exact bounded PML for the Helmholtz equation. *Comptes Rendus Mathématiques*, 339(11):803–808, 2004.

[31] A. Bermúdez, L. Hervella-Nieto, A. Prieto, and R. Rodríguez. Numerical simulation of time-harmonic scattering problems with an optimal PML. *Var. Formul. Mech.: Theory Appl.*, 13:58–71, 2006.

[32] A. Bermúdez, L. Hervella-Nieto, A. Prieto, and R. Rodríguez. An exact bounded perfectly matched layer for time-harmonic scattering problems. *SIAM Journal on Scientific Computing*, 30(1):312–338, 2007.

[33] A. Bermúdez, L. Hervella-Nieto, A. Prieto, and R. Rodríguez. Perfectly matched layers for time-harmonic second order elliptic problems. *Archives of Computational Methods in Engineering*, 17(1):77–107, 2010.

[34] B. Engquist and A. Majda. Absorbing boundary conditions for numerical simulation of waves. *Proceedings of the National Academy of Sciences*, 74(5):1765–1766, 1977.

[35] A. Bayliss and E. Turkel. Radiation boundary conditions for wave-like equations. *Communications on Pure and applied Mathematics*, 33(6):707–725, 1980.

[36] A. Bayliss, M. Gunzburger, and E. Turkel. Boundary conditions for the numerical solution of elliptic equations in exterior regions. *SIAM Journal on Applied Mathematics*, 42(2):430–451, 1982.

[37] A. Bayliss and E. Turkel. Far-field boundary conditions for compressible flows. *Journal of Computational Physics*, 48(2):182–199, 1982.

[38] R. Mittra, O.O. Ramahi, A. Khebir, R. Gordon, and A. Kouki. A review of absorbing boundary conditions for two and three-dimensional electromagnetic scattering problems. *IEEE Transactions on Magnetics*, 25(4):3034–3039, 1989.

[39] X. Antoine, H. Barucq, and A. Bendali. Bayliss-Turkel-like radiation conditions on surfaces of arbitrary shape. *Journal of Mathematical Analysis and Applications*, 229(1):184–211, 1999.

[40] D. Givoli. High-order local non-reflecting boundary conditions: a review. *Wave Motion*, 39(4):319–326, 2004.

[41] X. Antoine, C. Besse, and J. Szeftel. Towards accurate artificial boundary conditions for nonlinear PDEs through examples. *Cubo, A Mathematical Journal*, 11(4):1008–1033, 2009.

[42] D. Rabinovich, D. Givoli, and E. Bécache. Comparison of high-order absorbing boundary conditions and perfectly matched layers in the frequency domain. *International Journal for Numerical Methods in Biomedical Engineering*, 26(10):1351–1369, 2010.

[43] P. Bettess. Infinite elements. *International Journal for Numerical Methods in Engineering*, 11(1):53–64, 1977.

[44] P. Bettess. More on infinite elements. *International Journal for Numerical Methods in Engineering*, 15(11):1613–1626, 1980.

[45] O.C. Zienkiewicz, K. Bando, P. Bettess, C. Emson, and T.C. Chiam. Mapped infinite elements for exterior wave problems. *International Journal for Numerical Methods in Engineering*, 21(7):1229–1251, 1985.

[46] R.J. Astley and W. Eversman. Finite element formulations for acoustical radiation. *Journal of Sound and Vibration*, 88(1):47–64, 1983.

[47] R.J. Astley. Infinite elements for wave problems: a review of current formulations and an assessment of accuracy. *International Journal for Numerical Methods in Engineering*, 49(7):951–976, 2000.

[48] R.J. Astley and J.-P. Coyette. The performance of spheroidal infinite elements. *International Journal for Numerical Methods in Engineering*, 52(12):1379–1396, 2001.

[49] V. Villamizar, S. Acosta, and B. Dastrup. High-order local absorbing boundary conditions for acoustic waves in terms of far-field expansions. *Journal of Computational Physics*, 333:331–351, 2017.

[50] I. Harari and R. Djellouli. Analytical study of the effect of wave number on the performance of local absorbing boundary conditions for acoustic scattering. *Applied Numerical Mathematics*, 50(1):15–47, 2004.

[51] K. Schmidt and C. Heier. An analysis of Feng's and other symmetric local absorbing boundary conditions. *ESAIM: Mathematical Modelling and Numerical Analysis*, 49(1):257–273, 2015.

[52] T. Strouboulis, R. Hidajat, and I. Babuška. The generalized finite element method for Helmholtz equation. Part II: Effect of choice of handbook functions, error due to absorbing boundary conditions and its assessment. *Computer Methods in Applied Mechanics and Engineering*, 197(5):364–380, 2008.

[53] M. Dinachandra and S. Raju. Plane wave enriched partition of unity isogeometric analysis (PUIGA) for 2D-Helmholtz problems. *Computer Methods in Applied Mechanics and Engineering*, 335:380–402, 2018.

[54] T. Khajah and V. Villamizar. Highly accurate acoustic scattering: Isogeometric Analysis coupled with local high order Farfield Expansion ABC. *arXiv preprint arXiv:1810.09448*, 2018.

[55] E. Atroshchenko, C. Anitescu, T. Khajah, and T. Rabczuk. Isogeometric collocation in acoustics. 2018.

[56] D. Colton and B.D. Sleeman. Uniqueness theorems for the inverse problem of acoustic scattering. *IMA Journal of Applied Mathematics*, 31(3):253–259, 1983.

[57] J.-C. Nédélec. *Acoustic and electromagnetic equations: integral representations for harmonic problems*, volume 144. Springer Science & Business Media, 2001.

[58] F. Ihlenburg. *Finite element analysis of acoustic scattering*, volume 132. Springer Science & Business Media, 2006.

[59] T. Huttunen, P. Gamallo, and R.J. Astley. Comparison of two wave element methods for the Helmholtz problem. *Communications in Numerical Methods in Engineering*, 25(1):35–52, 2009.